

Monte Carlo and Navier–Stokes Simulations of Compressible Taylor–Couette Flow

Bénédicte Larignon,* Kevin Marr,† and David B. Goldstein‡
 University of Texas at Austin, Austin, Texas, 78712

The compressible Taylor–Couette flow between concentric cylinders, in the case where the inner cylinder rotates and the outer one is at rest, has been computed using direct simulation Monte Carlo (DSMC) and direct numerical simulation (DNS) methods. Depending on the air gap pressure, the flow in between the cylinders may be characterized by a variety of flow regimes ranging from free molecular to continuum and by the presence or absence of toroidal vortices. DSMC results for low- and intermediate-pressure cases (~ 10 – ~ 100 Pa), and DNS results for the intermediate- and high-pressure cases (~ 100 – ~ 1000 Pa) are compared to new experiments. In the DSMC simulations, as the Taylor number increases from 1 to 50, the velocity slip at the wall decreases from 10% to virtually no slip. In the DNS simulations, at high-pressure Taylor vortices are present in the gap, and the axially averaged nearly linear velocity profile evolves into an S-shape profile whereas the parabolic temperature profile becomes flatter in the center of the gap. The torque required to rotate the inner cylinder and the heat flux to the walls are compared to experiments. Agreement is good over the entire range of Taylor numbers.

Nomenclature

c_m	=	torque coefficient
d	=	gap width
H_{gap}	=	axial gap width
Kn	=	Knudsen number
P_2	=	pressure at outer cylinder
Re	=	Reynolds number, $\equiv \rho_2 U_1 R_1 \mu_2^{-1}$
R_1	=	radius of inner cylinder
R_2	=	radius of outer cylinder
r	=	position in radial direction
Ta	=	Taylor number, $\equiv \rho_2 U_1 d \mu_2^{-1} (d/R_1)^{1/2}$
T_{axial}	=	axial gap torque
$T(r)$	=	temperature at radial position r
T_1	=	temperature of inner cylinder
T_2	=	temperature of outer cylinder
U_1	=	tangential velocity of inner cylinder
$u(r)$	=	tangential velocity at radial position r
$\bar{u}(r)$	=	mean tangential velocity
z	=	position in axial direction
κ	=	thermal conductivity
λ	=	molecular mean free path
μ	=	coefficient of viscosity
ν	=	kinematic viscosity
ρ_2	=	density at outer cylinder
$\tau_{r\theta}$	=	shear stress in radial direction, $\equiv \mu (\partial \bar{u} / \partial r)$
ω_1	=	angular velocity of inner cylinder
ω_2	=	angular velocity of outer cylinder

I. Introduction

TAYLOR–COUETTE flow between two concentric cylinders is a well-known and oft-studied fluid dynamic problem

prominent in the development of rotating machinery. Recent experiments of a high-speed flywheel system, where the inner cylinder, the rotor, rotates while the outer cylinder, the stator, is at rest, have been performed at the Center for Electromechanics at the University of Texas (UT-CEM).¹ Because of advances in composite materials, it is now feasible to build rotors that can sustain higher tip speed and, hence, higher Mach numbers. The experiments ran at high tip speed, up to Mach 2, and covered a wide pressure range. Because of viscous flow in the air gap between the rotor and stator, the pressure was kept low to reduce frictional losses. However, maintaining a pressure low enough to negate such effects may be impractical in mobile flywheel applications where there are air leaks through the bearings. For that reason, the flow regimes, ranging from free molecular to continuum, characterized by the presence or absence of steady toroidal vortices, have been studied in the present work.

Taylor² investigated the formation of vortices in viscous flow between rotating concentric cylinders. He found that if the flow reaches a particular Reynolds number, toroidal ring vortices begin to develop.² The development of Taylor vortices can be predicated by means of a Taylor number Ta , which is a nondimensional measure of the gap width times the Reynolds number Re . Depending on the value of the Taylor number, a flow can exhibit several flow states including simple laminar Couette flow, laminar Couette flow with either sinuous or straight steady Taylor vortices, laminar Couette flow with unsteady Taylor vortices, or turbulent flow superimposed on Taylor-like vortices.³ Transitions between these different flow modes correspond to changes in the torque and heating on the inner and outer cylinders. Hence, predicting these transitions becomes important.

In the machines envisioned, the gas pressure in the air gap will be reduced well below atmospheric. Because the gas has a low density, the molecular mean free path λ may be large relative to the gap width d ; therefore, the Knudsen number based on gap spacing, λ/d , may also be large. In this rarefied regime, the Navier–Stokes equations are no longer valid, and the Boltzmann equation is used to describe the resulting flow, characterized by velocity and temperature slip between the gas and the solid surfaces. The most common engineering approach for modeling such low-density flows is the direct simulation Monte Carlo (DSMC) method. In the DSMC method, flow properties such as temperature and velocity are determined by sampling a large number of simulated molecules. These molecules are systematically moved and are allowed to collide with each other and with the boundaries before being moved again.⁴ Several groups have used DSMC to explore Taylor–Couette flow in a rarefied or low-density gas. Rarefaction effects may significantly affect the development of Taylor–Couette vortices, but the flow regime has not

Presented as Paper 2005-965 at the AIAA 43rd Aerospace Sciences Meeting, Reno, NV, 10–13 January 2005; received 1 August 2005; accepted for publication 1 November 2005. Copyright © 2006 by the authors. Published by the American Institute of Aeronautics and Astronautics, Inc., with permission. Copies of this paper may be made for personal or internal use, on condition that the copier pay the \$10.00 per-copy fee to the Copyright Clearance Center, Inc., 222 Rosewood Drive, Danvers, MA 01923; include the code 0887-8722/06 \$10.00 in correspondence with the CCC.

*Research Assistant, Department of Aerospace Engineering and Engineering Mechanics; larignonb@mail.utexas.edu. Student Member AIAA.

†Research Assistant, Department of Aerospace Engineering and Engineering Mechanics; marrkc@umich.edu.

‡Professor, Department of Aerospace Engineering and Engineering Mechanics; david@cfdlab.ae.utexas.edu. Senior Member AIAA.

been fully explored by either computational or experimental methods. At larger Knudsen numbers, the flow characteristics become difficult to predict due to slip flow conditions at the rotor and stator walls. Riechelmann and Nanbu,⁵ for example, established good agreement between torques calculated from DSMC simulations and experimental data for Knudsen numbers ranging between 0.004 and 0.04. They also found that vortex development changes the velocity in the middle of the gap by 35% and increases the slip at the walls by 5%. In a follow-up study three years later, they simulated wavy Taylor–Couette flow, showing that the sinuous vortices move in an azimuthal direction and that the azimuthal wavelength corresponds to experimental observations.⁶ In a study by Stefanov and Cercignani,⁷ DSMC simulations clearly exhibit the onset of vortices at Taylor values higher than the incompressible critical value. In a separate investigation, Aoki et al.⁸ found that increasing the temperature difference between the surfaces of the cylinders increases the region of steady Couette flow.

Guaranteeing low pressures in the air gap is difficult, and the possibility of a gas leak is real. Therefore, high-pressure continuum cases are also considered. Generally, experiments cannot provide a complete description of the interaction of these vortex structures with the surface, and numerical simulation of the governing Navier–Stokes equations is necessary. The high-pressure regime is simulated using a compressible temporal direct numerical simulation (CTDNS) code obtained from the University of Arizona. Reference 9 describes the direct numerical simulations of flows in the continuum regime where the air gap pressure is above approximately 100 Pa. Numerous experimental and numerical studies have been developed to consider the influence of the geometry, the speed of the cylinders, the temperature of the walls, and the fluid compressibility on the onset of the instability. This onset is generally characterized by a critical Taylor number Ta_c , defined as the largest value of the Taylor number such that all of the axisymmetric disturbances in the flow are damped out. Swinney¹⁰ compiled values of the critical Taylor number obtained by different sources. This set of data showed that Ta_c decreases as the radius ratio increases. Chandrasekhar¹¹ determined that the critical Taylor number decreases as the rotation rate ratio, ω_2/ω_1 , decreases from 1 to 0. Hatay et al.¹² studied the influence of compressibility on the stability of the Couette flow between rotating cylinders. They found that, for a resting outer cylinder, compressibility stabilizes the modes of the instability in the case of a narrow gap but destabilizes the modes for a wide gap. Finally, in both cases, they noticed that heating the outer cylinder has a stabilizing effect on the modes of the instability.

The purpose of the present study is to understand the characteristics of the flow in the UT-CEM flywheel air gap and to predict the resulting torques and heat fluxes on the rotor and stator surfaces. The numerical simulations encompass the rarefied flow regime where stable laminar Couette flow is expected and the continuum flow regime where Taylor vortex formation occurs. The bulk of the simulations are meant to emulate flywheel spin tests of a generic compulsator configuration conducted by the UT-CEM with air gap pressures of 10, 100, and 1000 Pa (Ref. 1). The work may also be considered a baseline study preliminary to the examination of more complex flows involving, for example, corner flows, abrupt changes in rotor speed or gas pressure, solid surface textures, or contamination by lubricant vapors.

A. Theory

A shear flow develops in a fluid-filled gap between two coaxial differentially rotating cylinders. For our purposes, both cylinders are long, and the inner cylinder rotates at a constant angular velocity while the outer cylinder is stationary. For incompressible flow, a common form of the Taylor number is³

$$Ta = [(U_1 d)/\nu] \sqrt{d/R_1} \quad (1)$$

If the flow is incompressible and temperature variations are small (so that the transport coefficients are approximately constant), simple laminar cylindrical Couette flow occurs when the Taylor number is less than 41.3. The Couette flow is characterized by a nearly linear

velocity profile that spans the velocity range from zero at the stator to U_1 on the rotor surface.³ The tangential velocity $u(r)$ in the gap can be found by solving the Navier–Stokes equations¹³ as

$$u(r)/U_1 = (R_2/r - r/R_2)(R_2/R_1 - R_1/R_2)^{-1} \quad (2)$$

The tangential velocity profile is normalized by the surface velocity of the rotor, and the curve of the velocity profile is determined by the ratio of the radius of the inner cylinder R_1 and the outer cylinder R_2 . The radial position r is referenced from the axis of rotation.

To compute small temperature changes, the temperature at a point in the gap $T(r)$ resulting from viscous dissipation is¹³

$$T(r) - T_1 = \left\{ \frac{\mu U_1^2}{\kappa(T_2 - T_1)} \frac{R_2^4}{R_2^4 - R_1^4} \left(1 - \frac{R_1^2}{r^2}\right) \left[1 - \frac{\ln(r/R_1)}{\ln(R_2/R_1)}\right] + \frac{\ln(r/R_1)}{\ln(R_2/R_1)} \right\} (T_2 - T_1) \quad (3)$$

Above a Taylor number of 41.3, the laminar Couette flow becomes unstable. The resulting Taylor vortices are steady toroidal vortex cells having alternate rotation directions. As the Taylor number increases past 400, Taylor vortices develop unsteady three-dimensional motion, and eventually the flow becomes turbulent. For compressible flow, at elevated Mach numbers, the Taylor number ranges for each flow state may be different from those in the incompressible case.

B. Domain and Experimental Data

The domain of interest is the whole gap between the two finite concentric cylinders (Fig. 1). However, the flow physics in the radial and the axial gaps is very different, and the CTDNS and DSMC codes are presently only used to simulate the flow in the radial gap. The flow on the top and bottom of the rotor, or flow in the axial gap, is not simulated. However, to compare the numerical results to the experimental results, analytical formulas¹⁴ have been used to model the flow in the axial gap. Even so, it was found that the torque exerted by the flow in the wide axial gaps is generally small compared to the torque produced in the radial gap.

The experiments done by UT-CEM aimed to measure the torque and the temperature distribution about a high speed rotor in a stator structure. Hahne et al.¹ were using a composite flywheel that could sustain rotor speeds in excess of 40,000 rpm and rotor tip speeds of 900 m/s with pressure ranges from 10 to 1000 Pa in the radial gap. The different tests made with this flywheel varied in peak revolutions per minute (RPM), runtime, and operating pressure. A total of 12 tests, numbered tests 1–12, have been run with three different peak speeds of 15,000; 27,600; and 40,000 rpm and the three pressure levels of 10, 100, and 1000 Pa. Because of mechanical stress and thermal heating, the inner radius and the gap width are different at each RPM, whereas the axial gap width is constant at 0.0123 m. The cylinder height is 0.121 m, which gives an aspect ratio of the annular gap of about 40. The input parameters for the numerical simulations of Tests 3–12, presented in Table 1, have been extracted at one point in time near peak RPM from the time-varying experimental data.¹ Reference 1 provides the accuracy of the measurements in the experiments. Generally, the surface temperature is within 1°C;

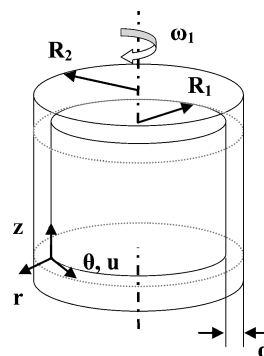
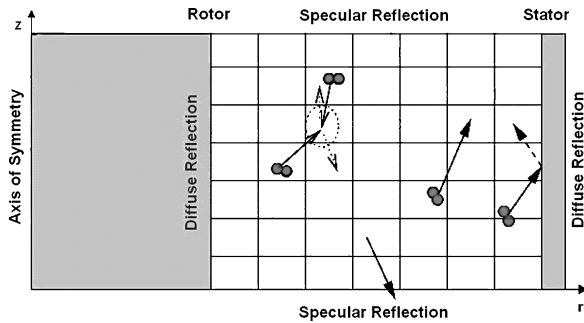


Fig. 1 Flywheel schematic with stretched scale for clarity.

Table 1 Experimental data used for simulations^a

Parameters	Unit	CEM test									
		3	4	5	6	7	8	9	10	11	12
Inner radius R_1	m	0.2125	0.2122	0.2122	0.2125	0.2125	0.2122	0.2125	0.2122	0.213	0.213
Gap width d	m	0.0031	0.0034	0.0034	0.0031	0.0031	0.0034	0.0031	0.0034	0.0025	0.0025
Radial gap pressure P_2	Pa	155	121	1463	1796	20	14.7	1746	13.3	26.7	241
Axial gap pressure P	Pa	113	106	1309	1317	9.3	8.0	1264	8.0	8.0	126
Rotor speed ω_1 or U_1	rpm	27600	15000	15000	27600	27600	15000	27600	27600	40000	40000
	m/s	614	333	333	614	614	333	614	333	892	892
Rotor temperature T_1	K	348	321	338	351	344	315	347	336	344	344
Stator temperature T_2	K	350	318	339	366	344	315	362	333	368	358
Taylor number Ta	—	17	10	107	181	3.6	1.6	179	1.5	5.0	27
Knudsen number Kn	—	0.011	0.013	0.001	0.001	0.086	0.108	0.001	0.118	0.080	0.009

^aCentrifugal and thermal stresses are accounted for in the rotor diameter. The radial gap pressure is measured in the middle of the radial gap at the stator whereas the rotor and stator temperatures are the average temperatures measured by multiple sensors in the radial gap.

**Fig. 2** DSMC computational domain.

the error range for the pressure is smaller than 0.05 torr; and, in a set of calibration tests, the measured torque is within 5% of the applied torque. More details on the experiments and the measurement techniques are presented in Ref. 1.

II. Computational Approach

A. DSMC^{15,16}

The DSMC method moves model molecules and samples molecular collisions to simulate a gas flow. The overall DSMC method is a sequence of move–collide operations described by Bird.⁴

The simulation area is an axisymmetric wedge in which the dominant mean flow is perpendicular to the simulation plane. The z axis of rotation is parallel to the axis of the cylinder and along the rotor surface; the r axis is positioned so that the positive direction is radially out. The sides of the domain are the inner and outer cylinder surfaces, and the top and bottom are planes of symmetry. Molecular collisions with the rotor and stator surfaces are governed by diffuse reflection at the respective surface temperatures: Molecular velocity after the reflection is independent of the velocity before the reflection (Fig. 2). The plane of symmetry boundaries are defined by specular reflection resulting in a mirror image of the flow about the boundaries. For the present purposes, molecular collisions are simulated with the variable hard sphere (VHS) model. In this VHS model, the velocity-dependent collision cross section is adjusted to produce the correct temperature exponent of the coefficient of viscosity of diatomic nitrogen gas.⁴ Moreover, the DSMC and DNS viscosities are matched in the overlap cases at intermediate pressures. To ease the DSMC calculations, the numerical gap is filled with simulated nitrogen even if the experimental gap is filled with air. A numerical comparison between the air- and nitrogen-filled gap showed that the resultant torque differs by less than 5%.

The simulation area is divided into identical rectangular cells to form the grid pattern. The radial span of each cell is no more than one mean free path, and the ratio of real molecules to simulated molecules (FNUM) is set so that there are approximately 10 simulated molecules per cell.

To initialize the flow, a mean number density corresponding to a measured pressure from each UT-CEM test is specified for the gas (ideal nitrogen). The rotor is given a certain surface velocity that is

applied as if the rotor instantaneously jumps to the specified speed at time zero.

Convergence for time-step size, steady state, and spatial grid resolution is verified for each run.

B. CTDNS Code

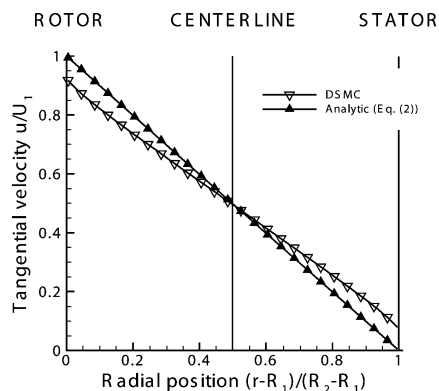
The CTDNS code used for the direct numerical simulations was developed at the University of Arizona.^{9,17} It solves the three-dimensional compressible Navier–Stokes equations in conservative form using a pseudospectral/finite difference approach in space and a Runge–Kutta scheme in time. Additional constitutive relations are employed to close the governing equations, namely, the equation of state for ideal gas for computing the pressure, the Newtonian fluid assumption for the viscous stress, Fourier heat conduction for the heat flux, and Sutherland’s law for the dependence of viscosity and conductivity on the temperature. The governing equations are solved in cylindrical coordinates inside the annular computational domain shown in Fig. 1 using a pseudospectral decomposition in the axial, z , and the azimuthal, θ , directions. In the radial direction r , sixth-order split compact differences are employed on a nonuniform grid with points clustered near the rotor and stator walls. An explicit fourth-order Runge–Kutta scheme is used for time advancement. Whereas in the axial and azimuthal directions periodicity is assumed for all flow variables, in the radial direction, at the rotor/stator boundaries, no-slip conditions for the velocities and isothermal boundary conditions for the temperature can be imposed. From the DSMC simulations, the velocity and temperature slips at intermediate pressures are found to be only 1–2%, which supports the use of no-slip conditions in the DNS simulations. A convergence study has been done and is presented in Ref. 9. Finally, whereas the growth rate of the small-amplitude disturbances depends on the size of the computational domain in the axial direction, the final results are independent of its size.

III. Results

The numerical results presented in this section are obtained once the flow reaches steady state. However, note that the numerical simulations differ from the experiments because both end effects and the time variation of the flow variables in the experiments are not taken into account. However, due to the large gap aspect ratio of 40 and the relatively steady experimental tip speed and radial gap pressure, the present simulations should model the experiments well. In the low-pressure cases up to 100 Pa, no vortices develop, and the parameters in the gap are only dependent on the radial position. In the high-pressure cases, the parameters also depend on the axial position, and they are plotted in the (r, z) plane. For a better comparison between low- and high-pressure results, axially averaged values of the parameters vs the radial position are also examined for the high-pressure cases. The profiles of the flow parameters are only plotted for one test case for each pressure range, each case being typical of each class of flow: test 7 for the low pressures, ~ 10 Pa; test 3 for the intermediate pressures, ~ 100 Pa; and test 6 for the high pressures, ~ 1000 Pa.

Table 2 Velocity gradient at 10 Pa

CEM test	Absolute value of velocity gradient = $\left \frac{\partial(u/U_1)}{\partial[(r-R_1)/(R_2-R_1)]} \right $		
	Center	Rotor	Stator
	7	0.8	1.2
8	0.77	1.2	1.2
10	0.76	1.1	1.1
11	0.81	1.3	1.3

**Fig. 3** Velocity profiles at 10 Pa (test 7).

A. Rarefied Couette Flow

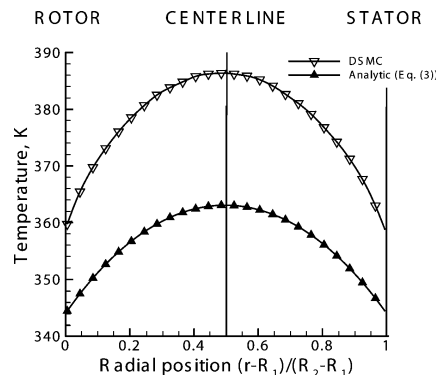
In this section, the results for the low-density regime at gap air pressures of about 10 Pa, in the tests 7, 8, 10, and 11, are presented. The Taylor number range for these simulations is 1–5, and the Knudsen number is about 0.1. Radial position and velocity are non-dimensionalized, but temperature is left in dimensional form to more easily visualize the temperature slip near the walls.

The velocity profiles are roughly linear across the narrow gap, but show an increased gradient near the rotor and stator surfaces (Fig. 3). Nondimensional velocity gradients are calculated by taking the slope of the velocity profiles at three locations along the gap: near the center of the gap, near the rotor surface, and near the stator surface (Table 2). The velocity gradients near the walls are approximately 50–60% larger than the gradient in the center of the gap. The DSMC simulations also show that the velocity near each surface slips or is different than the velocity of the surface itself. The amount of the velocity slip is quantified by comparing the velocity profiles to the no-slip analytical results. For all four low-pressure cases, the velocity slip ranges from 7–10% on both rotor and stator surfaces. However, tests 8 and 10 show slightly more velocity slip on both surfaces than tests 7 and 11.

The temperature profiles have a parabolic shape, with the maximum temperature near the center of the gap (Fig. 4). In the cases where the temperature is the same at each wall, the profiles are nearly symmetric, whereas in the cases with a temperature difference between the rotor and the stator the profiles are slightly off center. The relative steepness of the profiles also differs for each test case. For tests 8 and 10, the parabola is quite flat, where the maximum temperature is about 2–3% hotter than the near-stator temperature. For tests 7 and 11, however, the parabolic profile becomes steeper. Test 7 shows a temperature increase of 7% from near the stator to the center of the gap; test 11 shows a slightly larger temperature increase of about 13%. The temperature increase is defined as the percent difference between the maximum temperature in the gap and the temperature just near the stator wall. Similar to the velocity profiles, the temperature profiles also exhibit slip characteristics where the flow just near the surface is hotter than the surface itself. Table 3 shows the slip percentage at each wall for each test case. The slip percentage is defined as the percent difference between the temperature near the wall and the wall surface temperature. Tests 8 and 10 show similar slip results; the temperature slip near the

Table 3 Temperature slip at 10 Pa

CEM test	Temperature slip, %	
	Rotor	Stator
7	4.7	4.7
8	1.6	1.6
10	1.8	1.8
11	10.2	7.3

**Fig. 4** Temperature profiles at 10 Pa (test 7).

surface is close to 2% for both test cases. Compared to tests 8 and 10, the temperature slips about twice as much in test 7 and about 10 times more in test 11. Test 11 was the only simulation that exhibited significant slip asymmetry, where the temperature slip near the rotor was larger than the slip near the stator. However, note that, for test 11, the stator is about 20 K hotter than the rotor. The other low pressure simulations have only a small temperature difference between the rotor and stator.

B. Intermediate Pressure (100 Pa)

The intermediate pressure simulations, in tests 3, 4, and 12 are run with gap pressures around 100 Pa with Knudsen numbers of about 0.01, indicating nearly continuum flow. For that reason both CTDNS and DSMC simulations of these tests have been made. The corresponding Taylor number range for these tests is between 10 and 30 (Table 1). From the theory,³ a laminar Couette flow regime is expected for Taylor numbers less than 41.3 in incompressible flow. The CTDNS and DSMC numerical simulations exhibit, indeed, a laminar flow with no Taylor vortices present.

The comparison between the numerical results, both DSMC and CTDNS, with the analytical solutions provided by Eqs. (2) and (3) is presented in Figs. 5a and 5b for both tangential velocity and temperature. Similar to the low-pressure simulations, the profile for the tangential velocity is nearly linear, and the temperature profile is nearly parabolic with a maximum slightly closer to the hotter wall as seen in Figs. 5a and 5b. The agreement between the numerical results and the analytical solutions of Eqs. (2) and (3) is good. The CTDNS and analytical profiles are nearly the same for both temperature and velocity. However, the DSMC profiles exhibit temperature slip and a tiny velocity slip, which are not taken into account in either CTDNS or analytical results. For that reason, the DSMC velocity profile exhibits slightly steeper gradients at the walls, and the DSMC temperature profiles also present steeper gradients at the wall and a higher temperature in the middle of the gap.

Unlike the low-pressure tests, these velocity profiles do not show a significant velocity gradient increase near the two wall surfaces, and the velocity slip (about 1–2%) at each wall is much smaller. The velocity gradient is about 0.97 for all three medium pressure simulations. However, the temperature profile behavior at medium pressure is almost identical to that at low pressure. The profiles exhibit slip characteristics and increased temperature in the center of the gap (Table 4). Similar to the low-pressure temperature slip results, the temperature slip is nearly the same for both wall surfaces. Also, as the rotor tip speed increases, the temperature slip and temperature increase in the gap increase as well.

C. Taylor–Couette Flow with Vortices

Schlichting³ suggests that as the Taylor number in incompressible flow ranges between 41.3 and 400, laminar flow with Taylor vortices would be observed. For increased pressures around 1000 Pa, in the tests 5, 6, and 9, the Taylor numbers are in this range of values and Taylor vortices are found to be present in the CTDNS compressible flow simulations too. Figures 6a and 6b show contours of the tangential velocity in the (r, z) plane and its axially averaged profile

Table 4 Gap temperature behavior at 100 Pa

CEM test	Temperature slip, %		Temperature increase, %
	Rotor	Stator	
3	0.9	0.9	8.8
4	0.3	0.3	3.4
12	2.0	2.0	17.5

for test 6. In Fig. 6a, two vortices can be observed from the vector representation of velocity in (r, z) plane. The lower vortex turns clockwise and the upper one counterclockwise. In Fig. 6b, the laminar linear profile has evolved into an S-shape curve in the axially averaged flow due to the presence of vortices in the gap. The S shape of the velocity profile characterizes a flow with a higher gradient at the walls due to the mixing induced by the vortices and a nearly flat region where the axially averaged velocities are nearly constant in the middle of the gap.

In the higher-pressure cases, the axially averaged temperature profile exhibits two peaks, the highest of which is closer to the hottest wall (Fig. 7b). The shape in the center of the gap is much flatter than in the laminar flows. This averaged shape also exhibits steeper gradients at the walls, which will induce a higher heat flux. All of these changes are due to the presence of vortices that cause macroscopic radial mixing of the flow. In the case presented in Fig. 7a, the rotor is cooler than the stator. Between the vortex cores,

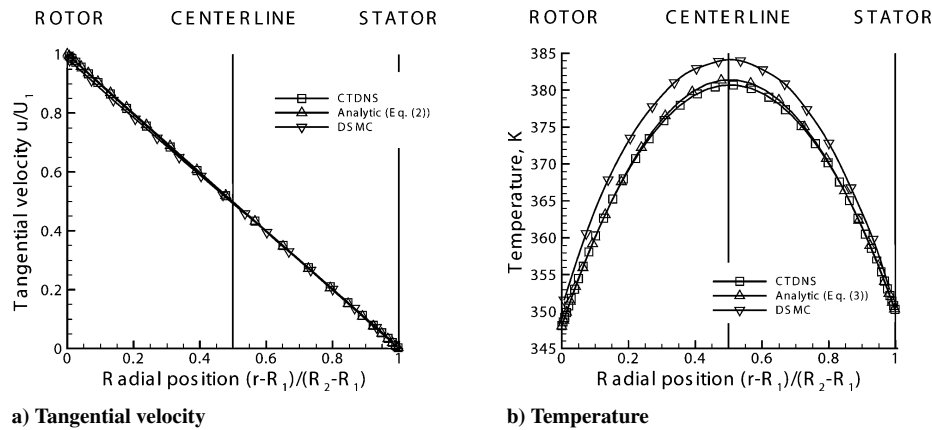


Fig. 5 Comparison of numerical and analytical profiles (test 3).

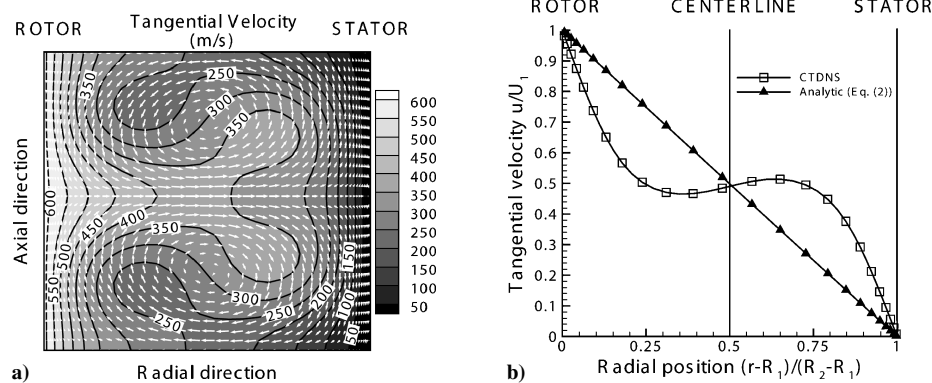


Fig. 6 Tangential velocity plots: a) tangential velocity contours in (r, z) plane and accompanying v and w velocity vectors and b) axially averaged tangential velocity profile compared to simple analytic results (test 6).

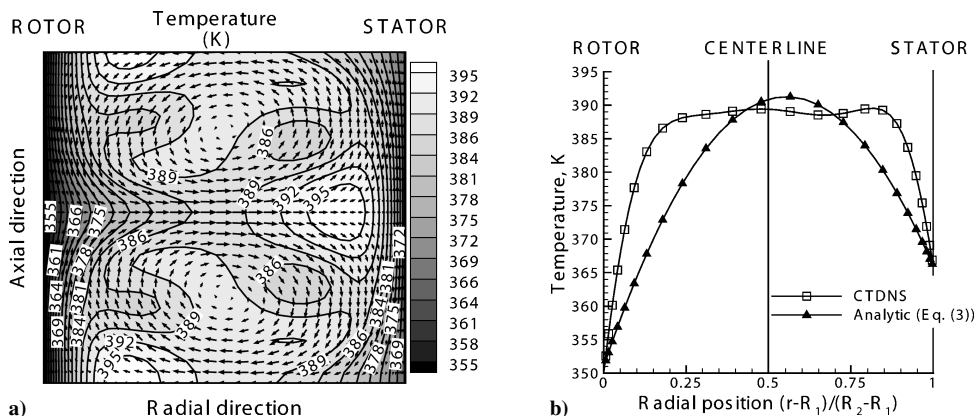


Fig. 7 Temperature plots: a) temperature contours in (r, z) plane and accompanying v and w velocity vectors and b) axially averaged temperature profile compared to simple analytic results (test 6).

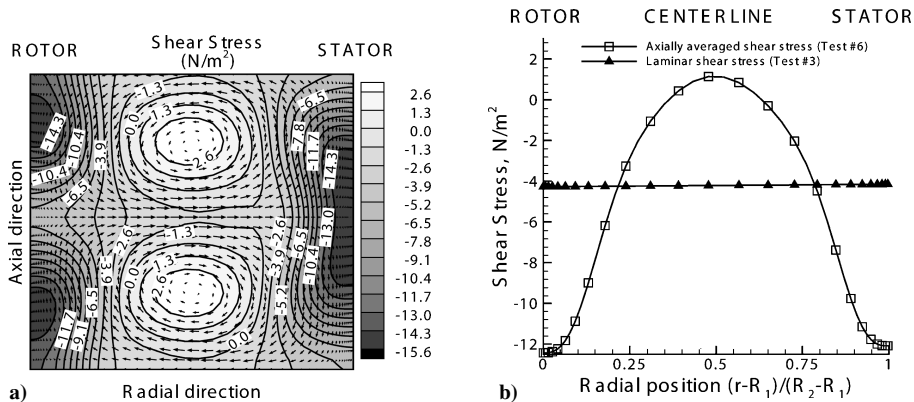


Fig. 8 Shear stress plots: a) shear stress $\tau_{r\theta}$ contours in (r, z) plane and accompanying v and w velocity vectors and b) axially averaged shear stress $\tau_{r\theta}$ profile (test 6) compared to laminar profile (test 3).

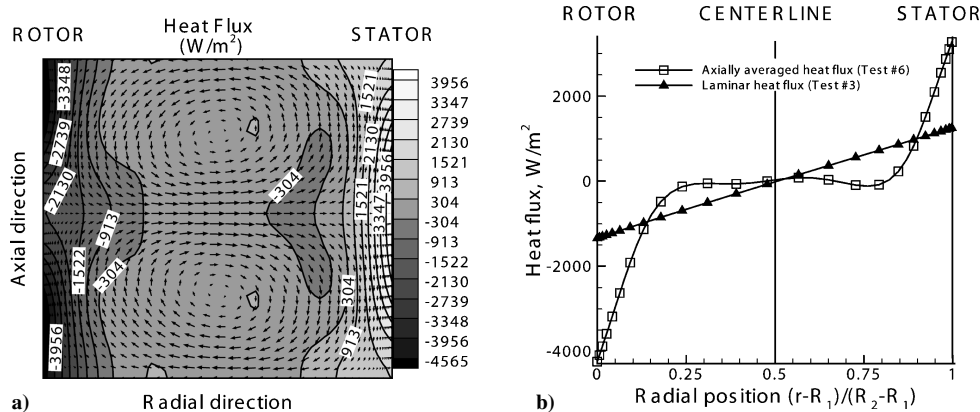


Fig. 9 Radial heat flux plots: a) radial heat flux contours in (r, z) plane and accompanying v and w velocity vectors and b) axially averaged radial heat flux profile (test 6) compared to laminar profile (test 3).

the vortices move the low-temperature fluid along the rotor wall toward the separation point in the middle of the gap. Simultaneously, at the top and bottom of the gap, the high-temperature particles closer to the stator are moved away from the stagnation point. Alternate layers of hotter and cooler fluid can then be observed in the (r, z) plane, and a mushroom form can be seen in the temperature contour. However, the shape obtained here is more complex than expected. For that reason, this simulation has been repeated a few times with various input temperatures and pressures and run for a long time. However, the results appear to confirm that the flow represented in Fig. 7a does not change, and the cause of this shape remains uncertain. A DSMC run has, however, not been made at this high pressure, but it would provide a comparison point for this contour.

The shear stress in the radial direction, $\tau_{r\theta}$, due to the mean tangential velocity, exhibits a sinusoidal shape for the high-pressure cases (Fig. 8b). Because of the increased gradient of the tangential velocity at the walls, the magnitude of the shear stress values at the wall is much higher in the high-pressure case. Yet, due to the general flatness of the velocity profile in the middle of the gap, the magnitude of the shear stress there is correspondingly small. Moreover, the values of the shear stress at the rotor and at the stator are slightly different. The amplitude of this difference is such that the torque is the same at both walls.

In Fig. 9a, the heat flux contour shows three distinct regions. The region in the center of the domain exhibits a heat flux close to zero. In the region close to the rotor, which is the coolest wall in this case, the heat flux is negative everywhere (into the rotor) but is not uniform along the wall. In fact, the region near the separation point on the rotor presents a nearly zero heat flux. As shown in the temperature contours (Fig. 7a), the vortices move the cooler fluid from the rotor and mix it with the hotter fluid present in the center of the gap. In the stagnation region where the midgap fluid is moved to the wall, the heat flux is larger. The heat flux profile shows an S shape for

Table 5 Torque calculations in Newton meters

CEM test	Radial gap only ^a		Radial and axial gap ^b		Measurement
	DSMC	CTDNS	DSMC	CTDNS	
3	0.161	0.146	0.226	0.211	0.198
4	0.072	0.065	0.097	0.090	0.086
5	—	0.166	—	0.254	0.244
6	—	0.423	—	0.643	0.705
7	0.119	—	0.140	—	0.147
8	0.051	—	0.062	—	0.068
9	—	0.420	—	0.637	0.703
10	0.056	—	0.067	—	0.070
11	0.233	—	0.261	—	0.254
12	0.316	0.268	0.436	0.388	0.424

^aRadial gap only values are obtained directly from numerical simulations where flow is only simulated between cylinder walls.

^bRadial and axial gap values are obtained by adding the torque at the bottom and top of the rotor, calculated using data from Ref. 14, to the radial gap only numerical values.

the higher-pressure cases. In the 1000-Pa cases, the flatter region in the center of the gap observed in the temperature profile (Fig. 7b) induces the S shape of the heat flux profile, whereas the higher-temperature gradients at the walls lead to higher values of heat flux at the walls compared to the lower-pressure cases.

D. Torque, Power, and Heat Flux: Comparison to Experiments

For each DSMC and CTDNS simulation, the torque and the heat flux at the walls are calculated and the torque is compared to the UTC-EM experimental results (Tables 5 and 6). The numerical torque only considers the radial air gap flow. However, the torque measured during the experiments also takes into account the torque due to the axial gap flow on the top and the bottom of the rotor. To compare the numerical results to the experimental ones, this axial gap

Table 6 Numerical heat flux at rotor and stator for each test case showing percentage of heat dissipated through each wall; tests 3, 4, 5, 6, 9, and 12 are from CTDNS runs, tests 7, 8, 10, and 11 are from DSMC runs

Heat flux, W/m ²	CEM test									
	3	4	5	6	7	8	9	10	11	12
To rotor q_1	1345	297	829	4171	2311	494	4114	509	3029	3721
To stator q_2	1259	329	766	3314	1930	474	3314	521	2680	3256

torque must be added to the numerical torque. An empirical solution given in Ref. 14 is used. In this book, some empirical methods are reviewed that can be used to estimate the torque on rotating disks and rotating cylinders using a curve fit to experiments. In our case, we are interested in modeling completely enclosed rotating disks to calculate the torque due to the axial air gap flow. For the axial gap torque, the Reynolds number and the ratio between the axial gap width H_{gap} and the rotor radius R_1 gives us the flow regime. We can then estimate the total torque coefficient and, finally, the torque. In the experiments, the ratio H_{gap}/R_1 is constant and is about 0.06. In this case, the torque is given by Eq. (4),

$$T_{\text{axial}} = c_m \rho_2 U_1^2 R_1^3 \quad (4)$$

where the torque coefficient is fit as follows. If $Re > 1500$,

$$c_m = 1.85(H_{\text{gap}}/R_1)^{1/10} / \sqrt{Re} \quad (5)$$

If $Re < 1500$,

$$c_m = \pi / (H_{\text{gap}}/R_1) Re \quad (6)$$

Note that Eqs. (4)–(6) involve the density at the stator. The density will be deduced from the pressure by using the perfect gas law. For the empirical calculations in the axial air gap, the pressure that is used is the pressure measured near the axis of the rotor.

The analytically adjusted DSMC torque results compare favorably with the experimental UT-CEM results. At 10 Pa, the DSMC simulations are at worst 8% (test 8), at best 3% (test 11), and on average 5% (tests 7 and 10) less than the experimental torque measurements. In general, the 100-Pa DSMC results did not agree quite as well as the 10-Pa results. At 100 Pa, DSMC tests 3 and 4 simulations overestimate the experimental torque by 10%. Test 12, however, shows excellent (within 1%) agreement with experiments.

The agreement between CTDNS and experimental results is better for the low rotor tip speed regime, $U_1 = 333$ m/s, for both low (test 4) and high (test 5) pressures. The results obtained in test 3 simulations also agree well with experiments where the velocity, $U_1 = 614$ m/s, and the pressure, $P_2 = 100$ Pa, are still low. In tests 6 and 9, the differences are greater, and the simulations underpredict the experimental torque.

Note that, in reality, however, the pressure in the axial gap should vary with the distance from the axis of the cylinders and fall between the measured axial and radial gap pressures. In the numerical calculations, the axial gap pressure is taken to be equal to the pressure measured close to the axis of the cylinders, which is smaller than the radial gap pressure due to a centrifugal pressure gradient. This might be one of the reasons why the numerical torque underpredicts the experimental results.

Table 6 shows that the heat flux is greater to the cooler wall, which is usually the rotor. Moreover, contrary to the torque results, the net heat flow may be different to the rotor and the stator. The conservation of energy in the simulations can be verified by comparing the power added to the flow through the torque on the rotor $P_{\text{radial flow}}$ with the heat flow to the walls $Q_1 + Q_2$. Here, the subscript radial flow indicates simply the portion due to radial gap flow. The power $P_{\text{radial flow}}$ is calculated using the torque results, whereas the heat flow to the wall is calculated using the heat flux simulations. By conservation of energy during steady-state operation, we should have $P_{\text{radial flow}} = Q_1 + Q_2$. The CTDNS results give only very small nonzero errors, within 1%, which are likely due to roundoff errors

during the dimensionalization or slight residual flow unsteadiness and not due to any flaw in the numerical dissipation.

IV. Conclusions

The low- and intermediate-pressure DSMC simulations are characterized by roughly linear velocity profiles, parabolic temperature profiles, and slip conditions at the rotor and stator surfaces. In the low-pressure cases, where the Knudsen number is about 0.1, the velocity profiles exhibit increased gradients near the wall surfaces and velocity slip at the 10% level. However, as the Knudsen number decreases to about 0.01 for the intermediate pressure cases, the DSMC simulations show that the velocity profile is nearly linear, and the velocity slip is an order of magnitude less than at the low pressures. For both low- and intermediate-pressure cases, the temperature behavior within the gap is qualitatively similar with the temperature slip at low pressure, being about five times larger than at intermediate pressure for corresponding rotor tip speeds. Moreover, as the rotor velocity increases by about 300 m/s, both pressure ranges show that the temperature slip and gap temperature difference approximately double. The DSMC/axial torque calculations agree reasonably well with experiments. At low pressures and Taylor numbers (1–5), DSMC underestimates the torque on average by 5%. At intermediate pressures (Taylor numbers between 10 and 30), DSMC overestimates the torque by about 10%. Note that our method does not account for the torque aberrations due to the corner flow. It is possible that the 5–10% discrepancy could be resolved by including the corner flow. Also, the axial gap calculation assumes a spatially uniform pressure (no gradients in the axial gap), which is not true for the actual machine.

The CTDNS simulations also agree well with the experimental results and give good insight into the nature of the flow. For the intermediate-pressure cases (tests 3, 4, and 12), the flow observed is laminar, and the results observed agree with the experimental and analytical results. The tangential velocity, as well as the shear stress and the heat flux profiles, exhibit a nearly linear shape, whereas the temperature profile can be characterized by a parabola with a maximum slightly closer to the hotter wall.

In the high-pressure cases (tests 5, 6, and 9), Taylor vortices are observed, and the axially averaged resulting profiles for each parameter evolves into more complex shapes. The tangential velocity, the shear stress, and the heat flux have S-shaped profiles with a flatter zone in the middle of the gap. The temperature parabola becomes flatter in the center of the gap. The contours of the different parameters in the (r, z) plane also give information about the different zones that can be considered in the flow. The core of the vortices is a zone where the shear stress may be positive. The stagnation points on the wall present a high temperature that results in larger heat flux and a greater magnitude of shear stress. On the other hand, the separation points exhibit reduced heat flux and shear stress. In all cases, the difference between the numerical and experimental torque does not exceed 13%.

In the future, the end effects due the finite size of the cylinders, as well as the flow in the axial gap, should be investigated to provide a better representation of the overall flow.

Acknowledgments

The authors gratefully acknowledge the University of Texas Center for Electromechanics for the partial funding of this research. We would like to also thank J. Zhang et al. for the use of their direct simulation Monte Carlo code and J. Zhang's helpful discussions.

References

- ¹Hahne, J. J., Werst, M., Penney, C., Liu, H. P., O'Harden, J., and Bogard, D., "Measurement of Windage Losses and Temperature Distribution for a High Speed Composite Rotor in a Stator Assembly at Low Air Pressures," 2003-47117, American Society of Mechanical Engineers, New York, July 2003.
- ²Taylor, G. I., *Mechanics of Fluids Miscellaneous Papers IV*, Cambridge Univ. Press, London, 1971, pp. 34–85.
- ³Schlichting, H., *Boundary-Layer Theory*, 7th ed., McGraw-Hill, New York, 1979, Chaps. 5 and 17.
- ⁴Bird, G. A., *Molecular Gas Dynamics and the Direct Simulation of Gas Flows*, Clarendon Press, Oxford, 1994, Chap. 10-15.
- ⁵Riechelmann, D., and Nanbu, K., "Monte Carlo Direct Simulation of the Taylor Instability in Rarefied Gas," *Physics of Fluids A*, Vol. 5, No. 11, 1993, pp. 2585–2587.
- ⁶Riechelmann, D., and Nanbu, K., "Three-Dimensional Simulation of Wavy Taylor Vortex Flow by Direct Simulation Monte Carlo Method," *Physics of Fluids*, Vol. 9, No. 4, 1997, pp. 811–813.
- ⁷Stefanov, S., and Cercignani, C., "Monte-Carlo Simulation of the Taylor-Couette Flow of a Rarefied Gas," *Journal of Fluid Mechanics*, Vol. 256, 1993, pp. 199–213.
- ⁸Aoki, K., Sone, Y., and Yoshimoto, M., "Numerical Analysis of the Taylor-Couette Problem for a Rarefied Gas by the Direct Simulation Monte Carlo Method," *Proceedings of the 21st International Symposium on Rarefied Gas Dynamics*, edited by R. Brun, R. Campargue, R. Gatignol, and J.-C. Lengrand, Vol. 2, CEPADUES, Toulouse, France, 1998, pp. 109–116.
- ⁹Larignon, B., Wernz, S., Goldstein, D., and Fasel, H., "Numerical Investigation of Vortex Onset in Supersonic Taylor-Couette Flow," *Journal of Thermophysics and Heat Transfer*, Vol. 20, No. 3, 2006, pp. 536–543.
- ¹⁰Swinney, H. L., *Hydrodynamic Instabilities and the Transition to Turbulence*, edited by H. L. Swinney and J. P. Gollub, Springer, Berlin, 1981, pp. 139–180.
- ¹¹Chandrasekhar, S., *Hydrodynamic and Hydromagnetic Stability*, Clarendon Press, Oxford, 1961, Chap. 7.
- ¹²Hatay, F. F., Biringer, S., Erlebacher, G., and Zorumski, W. E., "Stability of High-Speed Compressible Rotating Couette Flow," *Physics of Fluids*, Vol. 5, No. 2, 1993, pp. 393–404.
- ¹³White, F., *Viscous Fluid Flow*, 2nd ed., McGraw-Hill, New York, 1991, pp. 110–112.
- ¹⁴*The General Electric Fluid Flow Data Book*, Genium, New York, 1994.
- ¹⁵Zhang, J., Goldstein, D., Varghese, P., Gimelshein, N., Gimelshein, S., Levin, D., and Trafton, L., "DSMC Modeling of Gas Dynamics, Radiation and Fine Particulates in Ionian Volcanic Jets," *Proceedings of the 23rd International Symposium on Rarefied Gas Dynamics*, Vol. 663, edited by A. Ketsdever and E. Muntz, American Institute of Physics, Melville, NY, 2003, pp. 704–711.
- ¹⁶Zhang, J., Goldstein, D., Gimelshein, N., Gimelshein, S., Levin, D., and Varghese, P., "Modeling Low Density Sulfur Dioxide Jets: Application to Volcanoes on Jupiter's Moon Io," AIAA Paper 2001-2767, June 2001.
- ¹⁷Larignon, B., "Numerical Simulations of the Compressible Flow Between Concentric Cylinders Using an External Force Field in a Pseudo-Spectral Code," M.S. Thesis, Aerospace Engineering Dept., Univ. of Texas at Austin, TX, May 2004.